The effects of cubic stiffness on fatigue characterization resonator performance

M. Budnitzki [a,b], M.C. Scates [c], R.O. Ritchie [d], E.A. Stach [e], C.L. Muhlstein [c], O.N. Pierron [a,*]

[a] G.W. Woodruff School of Mechanical Engineering, Georgia Institute of Technology, 771 Ferst Drive, Atlanta, GA 30332-0405, USA
[b] Technische Universität Bergakademie Freiberg, Institute of Mechanics and Fluid Dynamics, Lampadiusstraße 4, D-09596 Freiberg, Germany
[c] Department of Materials Science and Engineering, The Pennsylvania State University, University Park, PA 16802, USA
[d] Department of Materials Science and Engineering, University of California, Berkeley, CA 94720, USA
[e] School of Materials Engineering and Birck Nanotechnology Center, Purdue University, West Lafayette, IN 47907, USA

ARTICLE INFO

ABSTRACT

Micromachined, kHz-frequency resonators are now routinely employed as testing structures to characterize the fatigue degradation properties of thin film materials such as polycrystalline silicon (polysilicon). In addition to stress-life (S–N) fatigue curves, important properties such as crack propagation rates may be inferred from proper resonant frequency measurements throughout a fatigue test. Consequently, any nonlinear dynamic behavior that would complicate the interpretation of resonant frequency changes should be avoided. In this paper, nonlinear frequency–response curves of a polysilicon fatigue structure are measured in a vacuum environment. Finite element models of the structure are used to identify the source of geometric nonlinearity leading to a Duffing-type cubic stiffness. Given the origin of the behavior, a parametric optimization strategy is performed to minimize the cubic stiffness. This study highlights the importance of considering the dynamic behavior when designing resonating structures, especially when they are used for mechanistic studies in various environments.

1. Introduction

The characterization of mechanical properties with micromachined resonators is a conceptually simple strategy, as long as the resonator's response is strictly linear. Provided that the material properties and geometry are well defined, analytical and finite element models can be applied to establish the natural frequencies of the structure. Then the changes in resonant frequency can be associated with damage accumulation [1–10], strength can be evaluated from the amplitude of motion at failure [2,11–14], and the differences in resonant frequency of arrays of devices with varying geometries can be used to establish the elastic modulus of the material [15]. However, nonlinear mechanical stiffness [16], nonlinear forcing functions [17–21], and other phenomena such as cracking [10] or residual stress in fixed–fixed beams [22] can induce nonlinear responses in the devices. For some applications, nonlinear dynamics can be exploited to improve the performance of MEMS sensors [19,23]. In the context of resonator-based fatigue testing of silicon thin films, however, linear behavior is preferred because it simplifies the analysis of fatigue crack growth [10,24]. As such, it is essential to have a clear understanding of why and when nonlinear behavior manifests itself in resonant characterization systems

so that it can be controlled and data are properly interpreted. The purpose of the present work is therefore twofold: highlight the risk of erroneous mechanistic interpretation when testing nonlinear MEMS fatigue resonators, and emphasize the value of assessing the occurrence of nonlinearities early in the design process using analytical and numerical models.

In this paper, a series of in vacuo measurements of a polycrystalline silicon (polysilicon) fatigue structure are presented (Section 2), where amplitude frequency–response curves exhibit nonlinear behavior (jump phenomenon) for large amplitudes. Two likely sources of nonlinearity are investigated using analytical and finite element models: structural nonlinearity and actuator nonlinearity (Section 3). Structural nonlinearity may arise when large displacements occur and is often described based on the Duffing-type behavior. Actuator nonlinearity may arise if the amplitude of the forcing function depends on the structure's displacement and can be modeled with the Mathieu equation. Material nonlinearity was not considered in this study, as micron-scale silicon does not deform plastically at room temperature (i.e., the constitutive behavior remains elastic) under bending load [25] and the deformations are small.[1] The corresponding simulations of the frequency–response curves are compared to experimental curves

---

* Corresponding author. Tel.: +1 404 894 7877; fax: +1 404 894 8496.
E-mail address: olivier.pierron@me.gatech.edu (O.N. Pierron).

[1] A maximum stress of 3.5 GPa corresponds to a strain of only about 2% in polysilicon with a Young's modulus of $E = 163$ GPa [26].
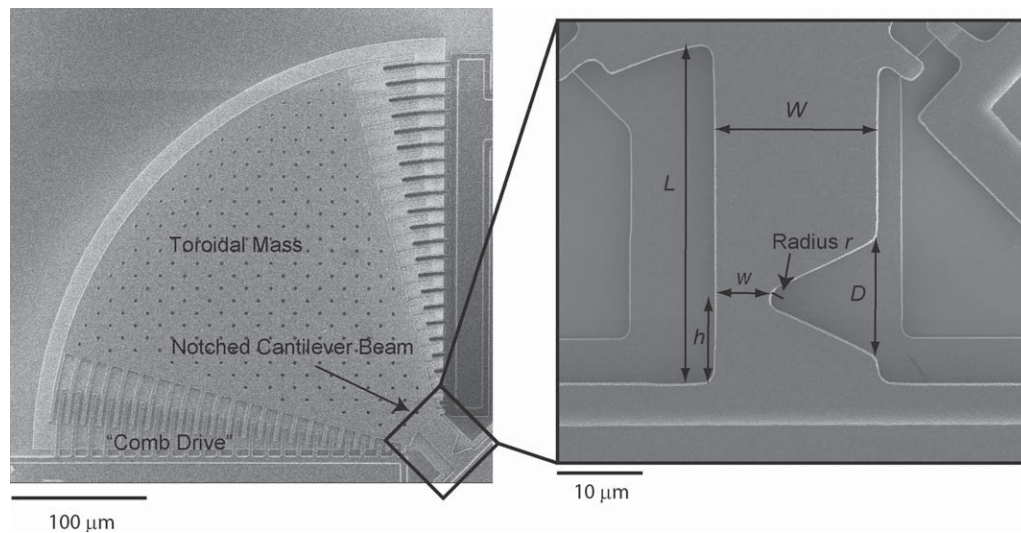
Fig. 1. Scanning electron micrographs of the polysilicon fatigue characterization structure employed in this study (detail of the notched cantilever beam on the right, along with the symbols used for its dimensions).

(Section 4), and the implications of nonlinear behavior on the accuracy of the measured fatigue properties are presented (Section 5) with recommendations for design improvement to minimize nonlinearities.

2. Experimental procedures

The fatigue characterization structures (see Fig. 1) employed in this investigation were surface-micromachined with the PolyMUMPs[TM] fabrication process (Run 18). The structure consists of a mass-spring rotational oscillator in the form of a fan-shaped mass connected to a notched, cantilever beam. At resonance, large stresses (~GPa range) can develop at the notch root of the beam. The maximum principal stress, σ_1, is proportional[2] to the amplitude of rotation of the structure; the constant of proportionality is calculated using finite element analysis, as described in Section 3.2. Twenty-two pairs of interdigitated fingers (comb drives) lay on each side of the mass to provide electrostatic actuation and capacitive sensing of the resulting motion. The fan-shaped mass spans 60° and has inner and outer radii of ~30 and 300 μm, respectively. The two comb drive arrays each span 15°, with a 5° overlap. The fan-shaped mass and comb drive arrays are attached to a substrate anchor via a notched cantilever beam (Fig. 1, inset). The center of rotation of the resonator that also defined the geometry of the comb fingers and fan-shaped mass is positioned at the center of the remaining ligament of the notched, cantilever beam. The critical dimensions that affect the structure's natural frequency and the maximum principal stress at the notch root are defined in Fig. 1. Specifically, the stiffness of the notched cantilever beam is a function of its length, L, its width, W, and the location and remaining ligament size (h and w, respectively) of the 60° opening-angle notch. Table 1 lists the measured dimensions based on high-magnification scanning electron micrographs. All measurements were made after the devices were released from the sacrificial oxide layer (2.5 min in 50% HF followed by 15 min in deionized H_2O, 5 min in isopropyl alcohol, and 1 min on a hot plate at ~110 °C) without further post-fabrication modifications such as organic monolayer or conductive coatings.

After release, the micromachined resonator was placed in a ceramic dual in-line package and a wire-bonder was used to make the electrical contacts that were necessary to drive the device. The packaged device was then transferred to a scanning electron microscope (JEOL 6340F SEM) for testing in vacuo. The structure was harmonically excited near resonance in the chamber at a pressure ranging between 0.19 and 0.28 mPa. Sinusoidal waveforms with four different amplitudes (2, 2.8, 4.8, and 5.6 V_{zp}) and no direct current (DC) offset were applied to one comb drive. The corresponding stress amplitudes ranged from ~0.2 to 1.6 GPa. For each amplitude, a series of high-magnification SEM images were taken at a specified location at the edge of the mass at different driving frequencies near resonance (~43 kHz) at 0.3 Hz increments. These frequency sweeps were performed in both directions (increasing and decreasing frequency values). The SEM images were used to measure the amplitude of motion (i.e., the angular rotation of the structure) in order to create the experimental frequency–response curves. The amplitudes of motion of the resonator at a given excitation frequency and driving voltage were measured from the width of the "blurred" edges of the fan-shaped mass and comb fingers using the software Scion Image (Scion Corporation, Frederick, MD). The pixel–distance correlation for each image was individually calibrated, and the averages of three measurements of the blurred edges at known positions on the resonator were then reported (see Fig. 2). This technique offers a lateral resolution of ~200 nm, resulting in a resolution of ~0.6 mrad in angular rotation (~3–5% of the measured value).

3. Modeling

This section details models of the dynamic behavior of the fatigue resonator (see Fig. 1). The governing differential equations and respective solutions are first presented for the cases of linear and nonlinear behavior. While a variety of phenomena can cause

Table 1
Measured beam dimensions (see Fig. 1).

Beam width (W)	19.3 μm
Beam length (L)	39.3 μm
Ligament width (w)	6.7 μm
Notch opening (D)	13.3 μm
Notch root radius (r)	1.4 μm
Notch height (h)	9.3 μm

---

[2] The effect of cubic stiffness, though crucial for the dynamic response, can be neglected in stress calculations.
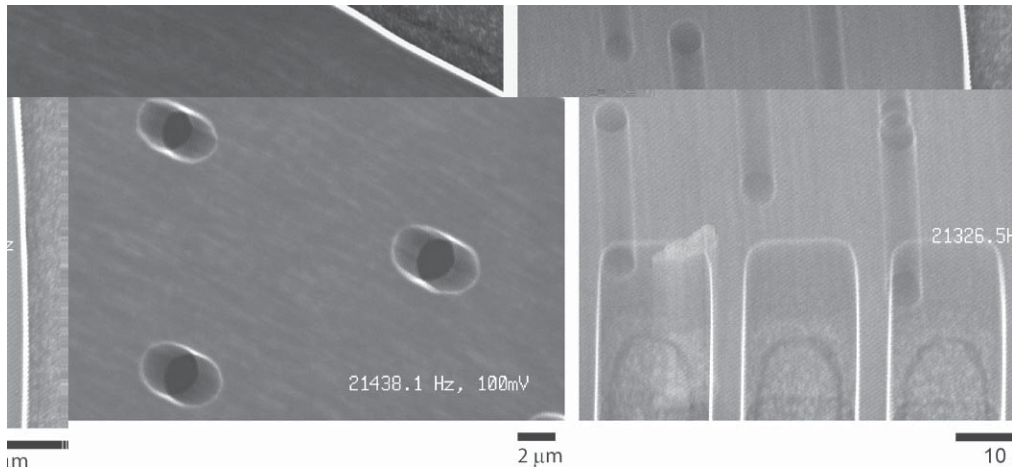
Fig. 2. Scanning electron micrographs of the polysilicon fatigue characterization structure near resonance. Similar images were used to measure the amplitude of rotation at a given frequency and driving voltage.

nonlinear behavior, this work considers cubic mechanical stiffness and parametric excitation. Finally, the geometrical model is parameterized to study the influence of critical geometrical features on the linearity of the response.

3.1. Governing equations

The fatigue oscillator can, to a first approximation, be modeled as a one-degree-of-freedom, harmonic, rotational oscillator whose governing second-order differential equation is:

$$J_\theta \ddot{\theta} + b\dot{\theta} + k_\theta \theta = M_0 \sin(2\pi ft) \tag{1}$$

where J_θ is the mass moment of inertia, b the damping coefficient, k_θ the linear torsional stiffness, M_0 the amplitude of the applied electrostatic moment, f is the frequency of the applied moment, and $\theta(t)$ is the angle of rotation of the structure about the midpoint of the remaining ligament of the notched beam. The amplitude of the applied moment is given by [10]:

$$M_0 = \frac{1}{4}\varepsilon h \sum_{j=1}^{44} \frac{1}{\ln(r_{o,j}/r_{i,j})} V_{in}^2 \tag{2}$$

where ε is the dielectric permittivity of vacuum, h the thickness of the structure (2 μm), $r_{o,j}$ and $r_{i,j}$ are the outer and inner radii of the jth capacitor formed by two adjacent fingers (22 pairs in this work), and V_{in} is the amplitude (zero-to-peak value) of the applied voltage. The numerical factor of 1/4 results from the forcing moment being a quadratic function of the applied sinusoidal waveform (the constant part of the forcing function is negligible on the overall response for lightly damped resonators, as is the case for the fatigue structure). The general form of the solution to Eq. (1) is given by:

$$\theta(t) = \frac{M_0}{k_\theta} \frac{f_0/f}{[(f_0/f - f/f_0)^2 + 1/Q^2]^{1/2}} \cos(2\pi ft - \delta)$$
$$= \Theta \cos(2\pi ft - \delta) \tag{3}$$

where f_0 is the undamped resonant frequency, δ is a phase shift due to the damping force, Θ is the amplitude of rotation, and Q is the quality factor defined by:

$$Q = \frac{f_0}{\Delta f} \approx \frac{2\pi f_0}{\gamma} \tag{4}$$

where Δf represents the full width at half-power (the amplitude at half-power points is approximately 70.7% of the peak amplitude) [27], and $\gamma = b/J_\theta$ is the damping ratio.

In the case of a nonlinear spring force with a cubic stiffness, Eq. (1) becomes Duffing's equation [28]:

$$J_\theta \ddot{\theta} + b\dot{\theta} + k_\theta \theta + k_{\theta 3} \theta^3 = M_0 \sin(2\pi ft) \tag{5}$$

where $k_{\theta 3}$ is the cubic stiffness coefficient. The corresponding amplitude of rotation Θ is given by the following frequency–response equation:

$$\left[\left(\frac{k_\theta}{J_\theta} - (2\pi f)^2\right)\Theta + \frac{3}{4}\frac{k_{\theta 3}}{J_\theta}\Theta^3\right]^2 + \left(\frac{b}{J_\theta}2\pi f\Theta\right)^2 = \left(\frac{M_0}{J_\theta}\right)^2 \tag{6}$$

Fig. 3 shows three representative curves for the linear case ($k_{\theta 3}$ = 0) and two nonlinear cases: hardening ($k_{\theta 3}$ > 0) and softening ($k_{\theta 3}$ < 0) nonlinearity. The bending of the frequency–response curves for the nonlinear cases leads to multivalued amplitudes and hence to the jump phenomenon that is illustrated in Fig. 3 for hardening nonlinearity. Let us consider an experiment where the frequency is slowly increased from an initial value $f < f_2$ (constant excitation): as the frequency is increased above f_2, the response follows the upper branch until the frequency f_1 is reached. A further
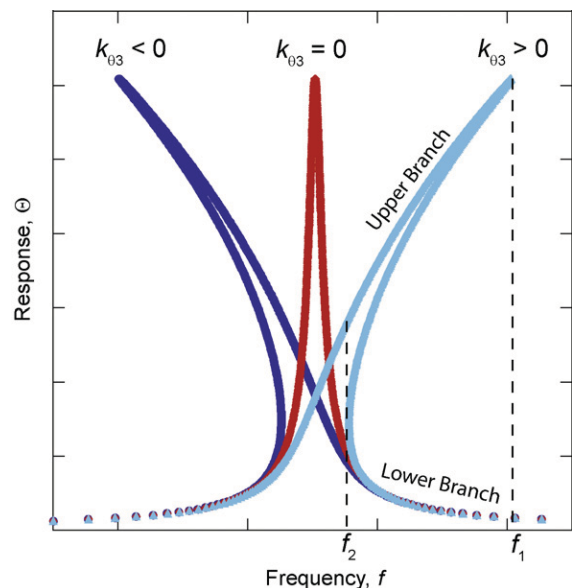

Fig. 3. Representative curves for the frequency–response equation: the linear case ($k_{\theta 3}$ = 0) and nonlinear hardening ($k_{\theta 3}$ > 0) and softening ($k_{\theta 3}$ < 0). Units are arbitrary.
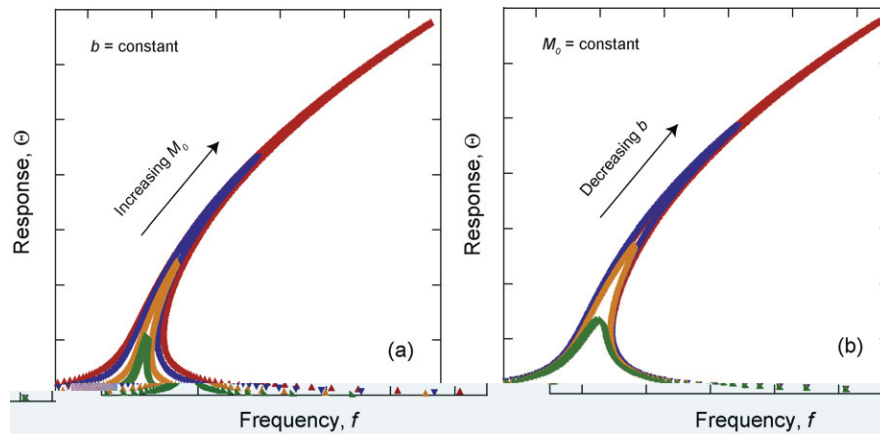
Fig. 4. Illustration of the influence of excitation (a) and damping (b) on Duffing's frequency–response curves (arbitrary units).

increase in frequency causes the response to jump to the lower branch. Conversely, if the frequency is slowly decreased from an initial value above f_1, the response remains on the lower branch until the frequency reaches f_2. Lowering the frequency further causes the response to jump to the upper branch. The apparent maximum response therefore depends on the direction in which the frequency is swept, which has important consequences for the testing of fatigue structures in vacuum (see Section 5).

Fig. 4(a) illustrates the influence of the applied moment on the resulting frequency–response curve, while Fig. 4(b) illustrates the influence of damping. In both cases, the frequency corresponding to the maximum response is given by the following equation:

$$f = \frac{1}{2\pi}\sqrt{\frac{k_\theta + (3/4)k_{\theta3}\Theta^2}{J_\theta}} \approx f_0\left(1 + \frac{3}{8}\frac{k_{\theta3}}{k_\theta}\Theta^2\right) \tag{7}$$

Another common origin of nonlinear effects is a nonideal excitation source. In the case of the fatigue structure shown in Fig. 1, a nonideal excitation may exist if the electrostatic forces depend on the angular rotation of the structure. Specifically, the electrostatic forces may increase for large angular rotation due to the proximity of the moving fingers' tips to the stator basis [29]. The corresponding governing equation is in that case is:

$$J_\theta\ddot{\theta} + b\dot{\theta} + k_\theta\theta = M_0(\theta)\sin(2\pi ft) \tag{8}$$

where $M_0(\theta)$ is the amplitude of the applied electrostatic moment that depends on the angular rotation. This differential equation cannot be analytically solved, and numerical strategies need to be applied (see for example [21] for a treatment of parametric excitation using the Mathieu equation).

3.2. Finite element modeling

A static analysis using the commercial finite element (FE) software ANSYS v. 11.0 was employed to study the (geometric) mechanical nonlinearity of the fatigue resonator due to large-deflection effects. 2D models of the entire structure (notched beam with the fan-shaped mass; see Fig. 1) were employed to calculate its (nonlinear) stiffness. A pressure was applied along one edge of the plate to simulate the moment applied via electrostatic forces while the displacements at the bottom of the beam were set to zero. The resulting motion of the structure was computed in a small strain, finite rotation analysis. Specifically, the NLGEOM,ON command [30] was issued to account for the geometric stiffness as well as follower forces [31], while the Saint Venant-Kirchhoff material with $E = 163\,$GPa, $\nu = 0.23$ [26] was used as constitutive relation. The geometry of the structure was fully parameterized to evaluate the stiffness of the PolyMUMPs$^{\text{TM}}$ 18 structure as well

as modified geometries. The measured critical dimensions of the PolyMUMPs$^{\text{TM}}$ 18 structure (see Table 1) were used, as opposed to nominal, "as-drawn" values. The meshing was performed using 8-node quadrilateral elements (PLANE 82) with the mesh density locally increased at the notch. The mesh was refined until convergence of the results was achieved.

4. Results

Fig. 5 shows the measured frequency–response curves of the fatigue structure (Fig. 1) in a vacuum environment ($P \sim 0.2\,$mPa), for four different driving amplitudes. At low signal amplitude (2 V), the curve is symmetric (quality factor Q equal to approximately 40,000). However, at higher amplitudes the measured behavior corresponds to that of a nonlinear oscillator. At 2.8 V the response curve is asymmetric, and a jump behavior develops at 4.8 and 5.6 V, as illustrated in Fig. 5 for the largest signal amplitude.

Previous studies performed on comb drives [29,32,33] indicate that the amplitude of applied moment (M_0) is fairly constant for θ less than 0.04 rad, above which it increases due to the electrostatic forces between the tip of the moving finger and the base of the stator. Since the nonlinear behavior was observed experimentally for maximum amplitude of rotation less than 0.02 rad (see Fig. 4), the origin of the nonlinearities cannot be parametric excitation.
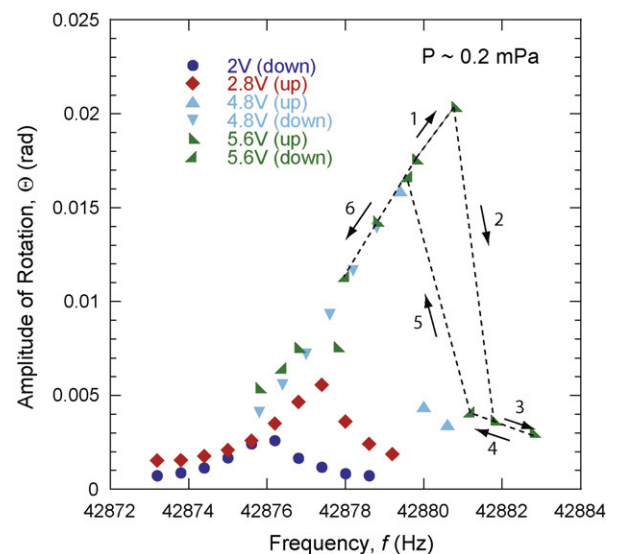

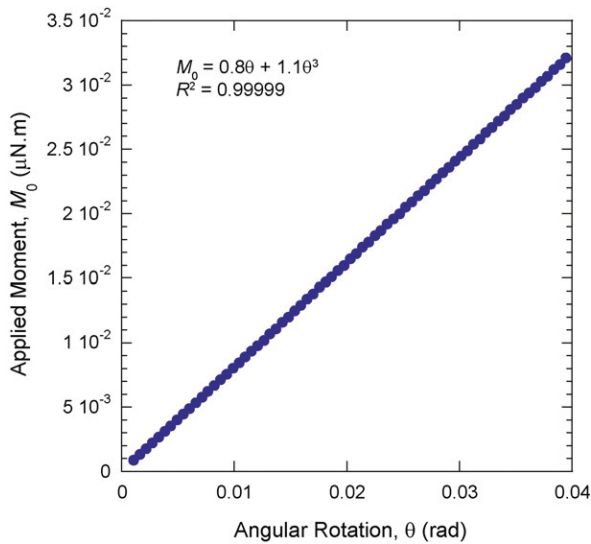**Fig. 5.** Measured frequency–response curves for the fatigue structure (see Fig. 1) tested in vacuo.

Fig. 6. Applied moment vs. rotation for the fatigue structure shown in Fig. 1, calculated using large-rotation finite element analysis.

Structural finite element analysis (see Section 3.2) was then used to calculate nonlinearity in the structure's stiffness due to large-rotation effects. The stiffness was found to increase slightly with increasing amplitude of motion (see Fig. 6), with corresponding linear and cubic stiffnesses of 8×10^{-7} N m rad^{-1} and 1.1×10^{-6} N m rad^{-3}, respectively. A positive cubic stiffness is qualitatively consistent with the observed behavior (bending of the frequency–response curve towards larger frequencies). These stiffness values were used to plot the frequency–response curve corresponding to Eq. (6). The moment of inertia was chosen to match the resonant frequency of the 2 V curve (see Fig. 5), and the damping coefficient was chosen to match the quality factor ($Q \sim 40,000$) obtained from experiment. The amplitude of the applied moment M_0 was calculated using Eq. (2). Fig. 7 superimposes the measured frequency–response curves on the ones calculated using Duffing's equation and the FEM-based stiffness parameters. A reasonable match is observed for the four different amplitudes. Specifically, the model predicts the jump frequencies f_1 and f_2 (see Fig. 3) to be $\sim 42,882.4$ and $42,878.3$ Hz, respectively, at 5.6 V, while the experimental results yield $f_1 = 42,881.5 \pm 0.5$ Hz and $f_2 = 42,880.5 \pm 0.5$ Hz. Similarly, the model predicts, at 4.8 V, $f_1 = 42,879.5$ Hz and $f_2 = 42,877.8$ Hz, while the experiments give $f_1 = 42,879.5 \pm 0.5$ Hz, and $f_2 = 42,879 \pm 1$ Hz. Given the experimental error bars associated with the limited number of data points,

the match appears reasonable. In addition, the model underestimates the maximum amplitude of rotation by $\sim 25\%$. There are a couple of reasons that can account for the aforementioned discrepancies between the model and the experimental results. First, the model assumes the same quality factor [i.e., same damping coefficient, b; see Eq. (4)] between the different frequency–response curves. Experimentally, the pressure may have changed between the different runs ($P \sim 0.2$ mPa), which can lead to some error in the curves as highlighted in Fig. 4b. Second, there may be some imprecision (estimated to be less than $\sim 5\%$) in the actual voltage amplitude applied to the MEMS device. A custom-made amplifier with a nominal gain of 20 was used. This incertitude in the applied voltage (and therefore in applied moment M_0; see Eq. (2)) may also affect the shape of the frequency–response curves, as highlighted in Fig. 4a. We therefore conclude that the observed nonlinear behavior of the fatigue characterization structure in vacuum is most likely a result of the geometric nonlinearity.

The influence of the beam's geometry on the resulting nonlinearity was captured with further finite element modeling in order to optimize the fatigue structure. The optimization of the device geometry has the objectives of (i) a frequency–response curve that is free from Duffing-type behavior, (ii) a maximum applied stress that is in excess of the material's ultimate strength for amplitudes of rotation less than 0.04 rad (to avoid nonlinearities due to parametric excitation in the current comb drive design), and (iii) a resonant frequency on the order of tens of kHz so that $\sim 10^9$ cycles can accumulate in less than a day of testing. Fig. 8 shows the calculated linear [Fig. 8(a)] and cubic [Fig. 8(b)] stiffnesses as a function of the ligament width (w) for three different notch root radii (r). As expected, the linear stiffness decreases with decreasing ligament width. The cubic stiffness decreases as well, but at a faster rate than the linear stiffness. Therefore, decreasing the ligament width should reduce the nonlinear behavior. Fig. 9 compares the frequency–response curves for a modified geometry ($r = 1.1 \mu m$, $w = 4.8 \mu m$) and the PolyMUMPs^{TM} 18 geometry ($r = 1.4 \mu m$, $w = 6.8 \mu m$). The amplitudes of the applied moments were chosen to obtain the same maximum rotation for both geometries and all other parameters from Eq. (6) were identical. The Duffing-type behavior clearly disappears with the modified geometry as a result of the relative decrease of the cubic stiffness with respect to the linear stiffness, albeit with a slight decrease in resonant frequency (~ 30 kHz instead of ~ 40 kHz). Although the dynamic behavior is improved by altering the geometry, the local maximum stress at the notch must be sufficiently large for testing to be viable. The relationship between the maximum principal stress at the notch root and the rotation of the structure was calculated for both geometries. Sufficiently large maximum principal stresses, σ_1,
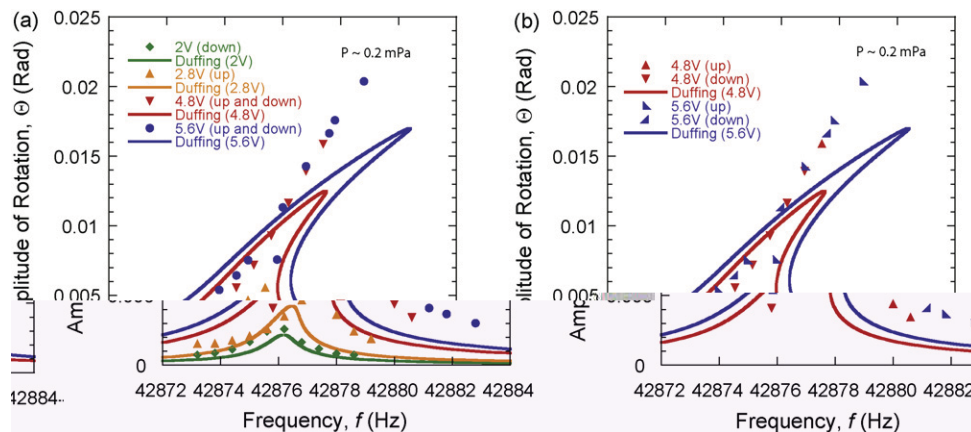

Fig. 7. Superposition of the measured and predicted (based on the Duffing's equation and finite element modeling of the fatigue structure) frequency–response curves.
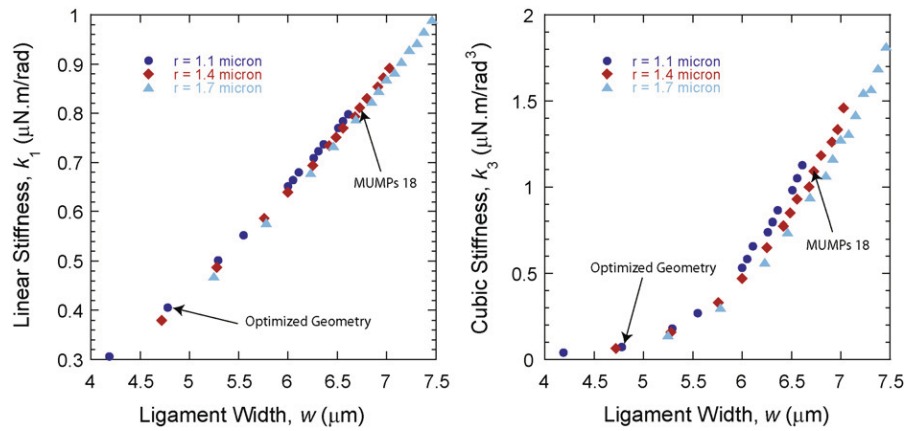
Fig. 8. Linear and cubic stiffnesses of finite element models of the fatigue structure for different notch root radii and ligament widths.
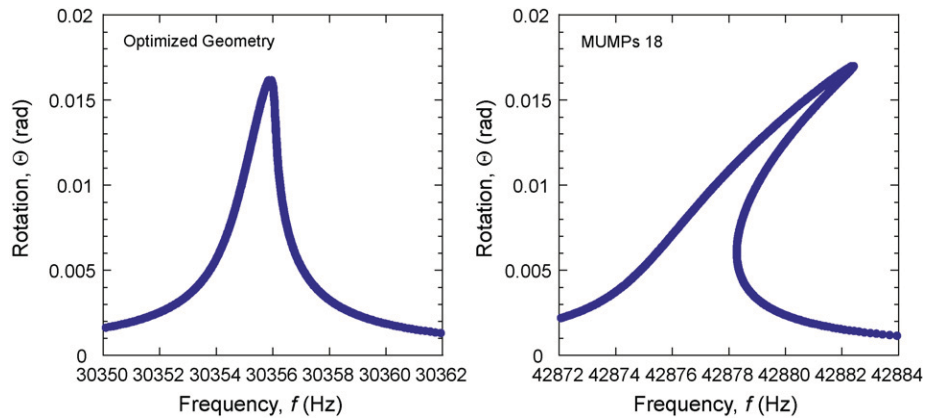

Fig. 9. Frequency–response curves using Duffing's equation for the fatigue structure geometry used in this study (right, $w = 6.8 \,\mu$m, $r = 1.4 \,\mu$m), and a proposed geometry (left, $w = 4.8 \,\mu$m, $r = 1.1 \,\mu$m) for which the nonlinear behavior is significantly reduced.

up to 3–3.5 GPa (see Fig. 10) can be applied at the notch for the modified geometry without reaching another nonlinear regime related to parametric excitation (which may happen for amplitudes larger than 0.04 rad). This optimized geometry is preferred when studying the fatigue degradation properties of polysilicon in vacuo because

Fig. 10. Maximum stress vs. angular rotation for two fatigue structure geometries whose frequency–response curves are shown in Fig. 8.

the evolution of resonant frequency is not obscured by nonlinear effects.

5. Implications for the mechanical testing of cantilever beam resonators

The structures shown in Fig. 1 were designed for fatigue testing of structural silicon thin films in air. These structures take advantage of the phenomenon of resonance to apply large sinusoidal stresses locally that cannot otherwise be applied via electrostatic actuation. Unlike conventional fatigue testing of bulk materials, the cracks developing and propagating at the notch of the structure cannot be directly measured due to their small physical size (tens of nm). However, resonant frequency measurements can be used to infer the crack propagation rates in these micron-scale fatigue structures [4,7]. Accordingly, any nonlinearity in the dynamic behavior will cause measurement artifacts and should be eliminated by changes to the device's geometry. In the case of the fatigue structure that developed a Duffing-type behavior when tested in vacuo (see Fig. 8), the following issues must be considered. First, the structures must be tested with the proper feedback loop to prevent unwanted unloading. Unloading may occur when testing at constant frequency (corresponding to the maximum response's amplitude) due to fatigue-related stiffness degradation that causes the peak of the device's frequency–response curve to shift towards lower values over time. This unloading phenomenon may result in inaccurate fatigue life measurements because the stress amplitude will not be constant [24]. Another issue is related to the measurement of the resonant frequency. Typically the resonant frequency
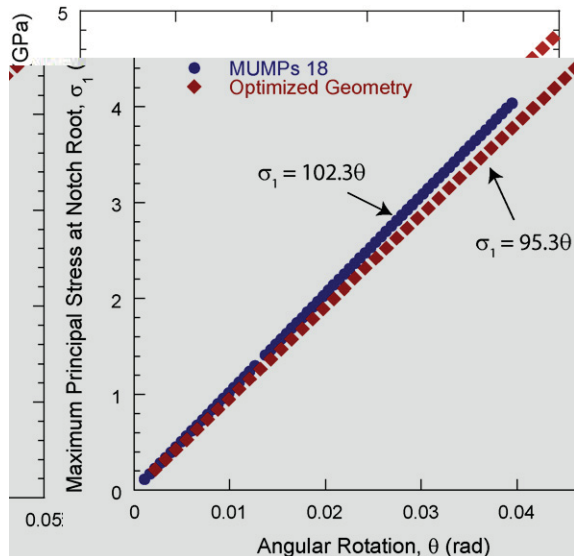
is experimentally obtained by electrically measuring the amplitude of displacement (via induced current measurements) as a function of frequency near resonance. The frequency corresponding to the maximum output (f_{max}) can be approximated as the resonant frequency (f_0) for linear resonators with large quality factors (Q). However, in the case of a hardening nonlinearity, f_{max} is related to f_0 via Eq. (7). The relative change in f_{max} (experimental measurement) does not correspond to the relative change in f_0, as shown in the following equation:

$$\frac{df_{max}}{f_{max}} = \frac{df_0}{f_0} - \frac{3}{8}\frac{\Theta_{max}^2}{k_\theta}\left(\frac{k_{\theta 3}}{k_\theta}dk_\theta - dk_{\theta 3}\right)$$

$$= \frac{1}{2}\frac{dk_\theta}{k_\theta} - \frac{3}{8}\frac{\Theta_{max}^2}{k_\theta}\left(\frac{k_{\theta 3}}{k_\theta}dk_\theta - dk_{\theta 3}\right) \tag{9}$$

The relative changes between the linear and cubic stiffnesses (k_θ and $k_{\theta 3}$) must be known a priori to deduce a relative change in the linear stiffness from the experimental measurements. An interesting consequence arising from Eq. (9) is that a relative decrease in linear stiffness (natural frequency) may occur while a relative increase in f_{max} is measured, when the following relation holds:

$$\frac{dk_{\theta 3}}{dk_\theta} < \frac{k_{\theta 3}}{k_\theta} - \frac{4}{3\Theta^2} \tag{10}$$

In that case, an increase in f_{max} should not be mistakenly interpreted as a stiffening of the structure (i.e., increase in k_θ). Such erroneous mechanistic interpretations that are based on resonant frequency measurements can be avoided by employing fatigue structures that display a linear dynamic behavior. The fatigue structure shown in Fig. 1 was successfully used to investigate the fatigue behavior at atmospheric pressures [1,4,5,7,9] but should be replaced with the geometry proposed at the end of Section 4 for fatigue studies in vacuum. Naturally, other resonating testing structures are vulnerable to similar effects.

6. Conclusions

This work demonstrated the need to study the dynamic behavior of MEMS fatigue resonators early in the design process, in order to prevent nonlinear structural behavior that may affect the mechanistic interpretation of the experimental results. Specifically, this paper investigated the nonlinear behavior of a micromachined resonator that has been used to characterize the fatigue behavior of polysilicon thin films. Frequency–response curves were experimentally obtained in vacuo based on high-magnification SEM images of the fatigue structure near resonance, and a jump phenomenon was identified. Finite element modeling was used to attribute the behavior to the nonlinear stiffness of the structure and to provide parameters that allowed Duffing's equation to be fitted to the general features of the experimental frequency–response curves. Further finite element modeling was employed to improve the design of the fatigue structure by eliminating the nonlinearity. The width of the notched beam at the notch was reduced, thereby limiting the nonlinear behavior in vacuo. Future in vacuo studies with resonators should use this or a similarly refined geometry.

References

[1] D.H. Alsem, et al., Fatigue failure in thin-film polycrystalline silicon is due to subcritical cracking within the oxide layer, Appl. Phys. Lett. 86 (4) (2005) 041914.

[2] D.H. Alsem, et al., Very high-cycle fatigue failure in micron-scale polycrystalline silicon films: effects of environment and surface oxide thickness, J. Appl. Phys. 101 (1) (2007) 013515.

[3] M. Budnitzki, O. Pierron, The influence of nanoscale atomic-layer-deposited alumina coating on the fatigue behavior of polycrystalline silicon thin films, Appl. Phys. Lett. 94 (14) (2009) 141906.

[4] M. Budnitzki, O.N. Pierron, Highly localized surface oxide thickening on polycrystalline silicon thin films during cyclic loading in humid environments, Acta Mater. 57 (10) (2009) 2944–2955.

[5] C.L. Muhlstein, S.B. Brown, R.O. Ritchie, High-cycle fatigue and durability of polycrystalline silicon thin films in ambient air, Sens. Actuators A 94 (2001) 177–188.

[6] C.L. Muhlstein, S.B. Brown, R.O. Ritchie, High-cycle fatigue of single-crystal silicon thin films, J. Microelectromech. Syst. 10 (4) (2001) 593.

[7] C.L. Muhlstein, E.A. Stach, R.O. Ritchie, A reaction-layer mechanism for the delayed failure of micron-scale polycrystalline silicon structural films subjected to high-cycle fatigue loading, Acta Mater. 50 (2002) 3579–3595.

[8] O.N. Pierron, C.L. Muhlstein, The critical role of environment in fatigue damage accumulation in deep-reactive ion-etched single-crystal silicon structural films, J. Microelectromech. Syst. 15 (1) (2006) 111–119.

[9] O.N. Pierron, C.L. Muhlstein, Notch root oxide formation during fatigue of polycrystalline silicon structural films, J. Microelectromech. Syst. 16 (6) (2007) 1441–1450.

[10] W.W. Van Arsdell, S.B. Brown, Subcritical crack growth in silicon MEMS, J. Microelectromech. Syst. 8 (3) (1999) 319–327.

[11] R.E. Boroch, et al., High-cycle fatigue and strengthening in polycrystalline silicon, Scr. Mater. 59 (9) (2008) 936–940.

[12] D. Broek, in: Martinus Nijhoff (Ed.), Elementary Engineering Fracture Mechanics, 4th ed., Hingham, Boston, MA, 1986.

[13] H. Kahn, et al., Fatigue failure in polysilicon not due to simple stress corrosion cracking, Science 298 (2002) 1215.

[14] H. Kahn, et al., Electrostatically actuated failure of microfabricated polysilicon fracture mechanics specimens, Proc. Roy. Soc. A 455 (1999) 3807–3823.

[15] L.M. Zhang, et al., Measurement of Young's modulus and internal stress in silicon microresonators using a resonant frequency technique, Meas. Sci. Technol. 1 (12) (1990) 1343–1346.

[16] S.G. Adams, et al., Independent tuning of linear and nonlinear stiffness coefficients, J. Microelectromech. Syst. 7 (2) (1998) 172–180.

[17] M. Agarwal, et al., A study of electrostatic force nonlinearities in resonant microstructures, Appl. Phys. Lett. 92 (10) (2008) 3.

[18] J.F. Rhoads, et al., Generalized parametric resonance in electrostatically actuated microelectromechanical oscillators, J. Sound Vibr. 296 (4–5) (2006) 797–829.

[19] K.L. Turner, et al., Five parametric resonances in a microelectromechanical system, Nature 396 (6707) (1998) 149–152.

[20] W.H. Zhang, R. Baskaran, K. Turner, Tuning the dynamic behavior of parametric resonance in a micromechanical oscillator, Appl. Phys. Lett. 82 (1) (2003) 130–132.

[21] W.H. Zhang, R. Baskaran, K.L. Turner, Effect of cubic nonlinearity on autoparametrically amplified resonant MEMS mass sensor, Sens. Actuator A-Phys. 102 (1–2) (2002) 139–150.

[22] K.B. Lee, A.P. Pisano, L. Lin, Nonlinear behaviors of a comb drive actuator under electrically induced tensile and compressive stresses, J. Micromech. Microeng. 17 (3) (2007) 557.

[23] B.J. Gallacher, J.S. Burdess, K.M. Harish, A control scheme for a MEMS electrostatic resonant gyroscope excited using combined parametric excitation and harmonic forcing, J. Micromech. Microeng. 16 (2) (2006) 320–331.

[24] C.L. Muhlstein, R.O. Ritchie, Fatigue of polycrystalline silicon for microelectromechanical system applications: crack growth and stability under resonant loading conditions, Mech. Mater. 36 (1–2) (2004) 13–33.

[25] D.H. Alsem, et al., Mechanisms for fatigue of micron-scale silicon structural films, Adv. Eng. Mater. 9 (1–2) (2007) 15–30.

[26] G. Simmons, H. Wang, Single Crystal Elastic Constants and Calculated Aggregate Properties: A Handbook, 2nd ed., M.I.T. Press, Cambridge, MA, 1971.

[27] J.H. Ginsberg, Mechanical and Structural Vibrations, John Wiley & Sons, Inc, 2001.

[28] A.H. Nayfeh, Nonlinear Oscillations, Wiley, New York, 1995.

[29] M.M. Tilleman, Analysis of electrostatic comb-driven actuators in linear and nonlinear regions, Int. J. Sol. Struct. 41 (18–19) (2004) 4889–4898.

[30] A.A. Research, Help System, Structural Analysis Guide, ANSYS Inc. Release 11.0.

[31] O.C. Zienkiewicz, in: R.L. Taylor (Ed.), The Finite Element Method for Solid and Structural Mechanics, 6th ed., Elsevier Butterworth-Heinemann, Amsterdam, 2005.

[32] W. Ye, S. Mukherjee, Optimal shape design of three-dimensional MEMS with applications to electrostatic comb drives, Int. J. Numer. Methods Eng. 45 (2) (1999) 175–194.

[33] W. Ye, S. Mukherjee, N.C. MacDonald, Optimal shape design of an electrostatic comb drive in microelectromechanical systems, J. Microelectromech. Syst. 7 (1) (1998) 16–26.